Distribution of active faulting along orogenic wedges: Minimum-work models and natural analogue

Daniel L. Yagupsky [a],[*], Benjamin A. Brooks [b],[1], Kelin X. Whipple [c], Christopher C. Duncan [d], Michael Bevis [e]

[a] Laboratorio de Modelado Geológico, Instituto de Estudios Andinos "Don Pablo Groeber" (IDEAN), Departamento de Ciencias Geológicas, FCEN, Universidad de Buenos Aires, BsAs C1428EGA, Argentina
[b] School of Ocean and Earth Science and Technology, University of Hawaii, 1680 East-West Rd., Honolulu, HI 96822, USA
[c] Schoolof Earth and Space Exploration, Arizona State University, Tempe, AZ, USA
[d] Department of Geosciences, University of Massachusetts, Amherst, MA 01002, USA
[e] Geodetic Science, Ohio State University, Columbus, OH, USA

ABSTRACT

Numerical 2-D models based on the principle of minimum work were used to examine the space-time distribution of active faulting during the evolution of orogenic wedges. A series of models focused on thin-skinned thrusting illustrates the effects of arid conditions (no erosion), unsteady state conditions (accretionary influx greater than erosional efflux) and steady state conditions (accretionary influx balances erosional efflux), on the distribution of fault activity. For arid settings, a general forward accretion sequence prevails, although a significant amount of internal deformation is registered: the resulting fault pattern is a rather uniform spread along the profile. Under fixed erosional efficiency settings, the frontal advance of the wedge-front is inhibited, reaching a steady state after a given forward propagation. Then, the applied shortening is consumed by surface ruptures over a narrow frontal zone. Under a temporal increase in erosional efficiency (i.e., transient non-steady state mass balance conditions), a narrowing of the synthetic wedge results; a rather diffuse fault activity distribution is observed during the deformation front retreat. Once steady balanced conditions are reached, a single long-lived deformation front prevails.

Fault activity distribution produced during the deformation front retreat of the latter scenario, compares well with the structural evolution and hinterlandward deformation migration identified in southern Bolivian Subandes (SSA) from late Miocene to present. This analogy supports the notion that the SSA is not in steady state, but is rather responding to an erosional efficiency increase since late Miocene.

The results shed light on the impact of different mass balance conditions on the vastly different kinematics found in mountain ranges, suggesting that those affected by growing erosion under a transient unbalanced mass flux condition tend to distribute deformation along both frontal and internal faults, while others under balanced conditions would display focused deformation on a limited number of steady structures.

© 2014 Elsevier Ltd. All rights reserved.

1. Introduction

Orogenic wedge models are important for geodynamics because they promote the analysis of orogenic systems as integral units, allowing the exploration of their evolution in terms of major tectonic controls. In this regard, the critical taper model (e.g., Dahlen, 1990) has proved to be a powerful vehicle for understanding the basic mechanics of orogenic wedges and the interaction of erosion and deformation (e.g., Koons, 1990; Barr et al., 1991; Willett et al.,

* Corresponding author. Tel.: +54 11 4576 3400.
E-mail addresses: daniely@gl.fcen.uba.ar, yagdaniel@gmail.com (D.L. Yagupsky).
[1] Now at Earthquake Science Center, US Geological Survey, 345 Middlefield Rd., Menlo Park, CA 94025, USA.

1993; Hilley et al., 2004; Whipple and Meade, 2004, 2006). This approach, however, only aims to capture the overall evolution of these systems, averaged in space and time, and has limited ability to shed light on the connections between long-term deformation patterns and individual structures. These connections, significantly influenced by stratigraphic and other heterogeneities, have been reproduced in both analog experiments and numerical models (e.g. Stolar et al., 2007; Stockmal et al., 2007; Del Castello and Cooke, 2007; Cubas et al., 2008; Mary et al., 2013a). In a time and space averaged sense, they do behave generally as expected according to the critical taper theory, but yet deviate from model predictions in several important aspects. For instance, rather than growing continuously, new material is generally seen to be episodically incorporated into the wedge via phases of frontal accretion and internal deformation (Gutscher et al., 1996; Adam et al., 2005; Hoth et al., 2006; Del Castello and Cooke, 2007; Stockmal et al., 2007; Mary et al., 2013a,b). This has significant, though underappreciated, implications regarding the interrelationships between the geologic, geomorphic, and geodetic records of deformation, and the spatial distribution of seismic activity. Particularly, the fault activity distribution during the orogenic belt growth is one of the most relevant unresolved aspects of the problem.

Surface processes and erosion play a key role in the evolution of active thrust wedges, as demonstrated by numerical modeling and approximate analytical solutions (e.g., Willett, 1999; Beaumont et al., 2001; Willett and Brandon, 2002; Hilley and Strecker, 2004; Whipple and Meade, 2006; Mary et al., 2013b). Recently, the concept of critical wedge has been applied to understand how increased precipitation-induced erosion influences an orogen's size, concluding that active orogenic wedges should shrink and rock uplift rates increase in response to an increase in erosional efficiency (Hilley and Strecker, 2004; Whipple and Meade, 2004; Stolar et al., 2006). Despite these advances, uncertainties remain regarding the expected fault activity distribution throughout the wedge under different mass balance conditions — i.e. whether a wedge is growing, shrinking, or at steady state.

In this paper, we present a new generation of numerical 2-D models based on the principle of minimum work (e.g., Masek and Duncan, 1998; Del Castello and Cooke, 2007) aiming to advance our understanding of the factors controlling strain distribution during the wedge's evolution. This is a middle ground approach between the analytic critical taper treatment, and mechanically more complex finite element models (e.g., Vanderhaeghe et al., 2003; Stockmal et al., 2007). While minimum work modeling lacks the rigor of more conventional force-balance modeling, previous efforts have shown this approach to be a good approximation for specific geodynamical systems, including thrust systems (Mitra and Boyer, 1986; Molnar and Lyon-Caen, 1988; Hardy et al., 1998; Masek and Duncan, 1998; Cooke and Murphy, 2004; Del Castello and Cooke, 2007). We consider these models particularly well suited to the object of our study, as they resolve the spatial and temporal variability of strain concentration, are computationally efficient, and can easily be coupled to realistic erosion laws (e.g., Whipple and Meade, 2004). An extended version of the Masek and Duncan code was developed in order to explore the potential distribution of discrete fault activity during wedge evolution, associated with both growing wedge (accretionary influx greater than erosional efflux) and steady state (accretionary influx balances erosional efflux) scenarios.

We compare horizontal shortening rates and the distribution of active faults obtained from our numerical simulations with the long-term deformation pattern across the southern Bolivian Sub-andes (SSA). The Plio-Quaternary shortening rate through this segment of the Central Andes is estimated to be ~7—13 mm/yr (Echavarria et al., 2003; Oncken et al., 2007; Uba et al., 2009), but

there is no consensus regarding how this shortening is distributed in space and time across the active thrusts of the system. Our models show that under unsteady mass balance conditions (a growing wedge), as inferred for the SSA (Brooks et al., 2011), active deformation would be distributed across a relatively wide frontal zone comprising ~40–50% of the total profile width, although most activity localizes on the frontal ~30% of the wedge. This is in good agreement with studies on the SSA which indicate that in addition to the known frontal faults, internal structures are currently active (Lamb, 2000; Echavarria et al., 2003; Mugnier et al., 2006; Uba et al., 2009), and probably have been so since Pliocene times (Echavarria et al., 2003; Ramos et al., 2004). Based on this analogy, we discuss the way in which the transient unsteady mass balance conditions may modulate the observed distribution of active thrusts.

2. Minimum-work method

Minimum-work and minimum dissipation are examples of variational principles, which suppose that the minimization or maximization of some quantity (e.g., work) over an entire physical system will replicate the dynamics given by conventional Newtonian analysis. Difficulties arise when dealing with complex, nonlinear systems, for which it is often impossible to prove analytically a correspondence between variational and Newtonian principles, or to identify a unique variational function to be minimized or maximized (Finlayson and Scriven, 1967). As noted by Sleep et al. (1979), this fact does not necessarily imply that variational principles are poor approximations to geologic systems (see Masek and Duncan, 1998 for further discussion). In Masek and Duncan (1998), a good correlation between minimum-work wedge models and the Coulomb critical wedge approximation of Dahlen (1990) have been found, confirming a direct correlation between topographic slope and the friction coefficient. However, given that the minimization principle reflects fundamental shortcomings inherent in using approximate methods, results should be interpreted conservatively.

In this paper, the principle of minimum work is applied to assess the relative efficiency of alternative paths of deformation. During the evolution of a fold and thrust belt certain faults initiate while others shut down. This behavior responds to the interplay of different work terms while the system continually seeks to minimize the total work ($Wtot$) associated with the creation of and movement along fault paths. $Wtot$ is the sum of the following terms: work against gravity due to the lifting of columns of material above ramps (W_{grav}), work against frictional sliding due to slip on the fault surface (W_{fric}), work of internal deformation of the material around the fault (W_{int}), work of propagating new faults (W_{prop}), and work of seismic radiated energy (W_{seis}) (Cooke and Murphy, 2004). We follow Mitra and Boyer (1986), Williams (1987) and Scholz, 2002) in assuming that $W_{int} + W_{prop} + W_{seis} << W_{fric} + W_{grav}$, allowing us to assume that

$$Wtot \sim Wfric + Wgrav \tag{1}$$

The numerical code used in this paper is an improved version of the one used by Masek and Duncan (1998), incorporating updates that render a more realistic erosion law. The model comprises a two-dimensional cross section through the crust, represented as a Cartesian grid of nodes in a vertical plane (Fig. 1) subjected to an incremental shortening Δx per time step. The shortening is accommodated by movement along a through-going fault trace formed by linking nodes in adjacent columns into a continuous path from a starting node at depth up to the surface. The particular path chosen at each time step is the one whose W_{tot} is the smallest
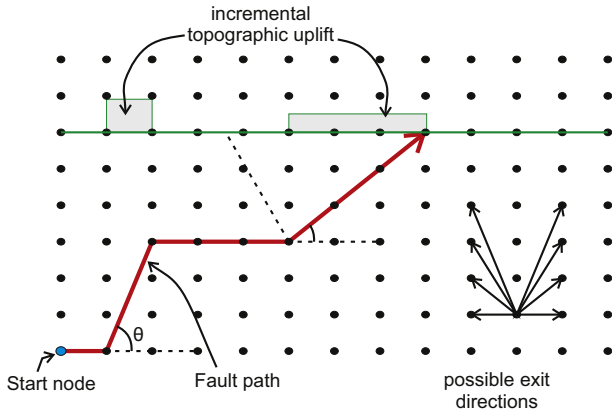
Fig. 1. Schematic example of model grid. Start node (light blue circle) at the lower left corner of the grid. Eight exit directions are allowed from each node. Red arrow indicates an active fault-path through the grid for a single time-step; grey areas show zones of incremental rock uplift resulting from this path. A kink axis is shown with dotted line.

of all possible paths. Each node in the grid is linked to a number of nodes in the two adjacent columns using a prescribed set of allowed "exit directions" that a fault may follow to the next node on the path (Fig. 1). These exit directions constrain the through-going fault path such that it can cut horizontally or upward, but never down to a greater depth. Faults are also constrained to originate at a prescribed "start node", to continue all the way to the surface, and never to double-back on themselves. Therefore, there is a single point from which all fault paths must originate. This constraint is identical to the geometry of a physical sandbox model, where all faults must eventually meet the junction between the backstop and the lower boundary. Work is associated with motion on the links: if the link is horizontal, there is only W_{fric}; for links that are inclined, there are both W_{fric} and W_{grav} terms.

At each time step we use Eq. (1) to compute the work terms for every possible link in the grid, then use those results to compute the minimum total work to get from each node to the surface via every allowed exit direction. In the case of ties, a random choice is taken among the tied directions, so two models with the same initial parameters can evolve using slightly different fault paths; this occurs primarily at the start of a run when no topography is present and has a negligible effect on the long-term evolution of the system. Although the incremental shortenings are accommodated using the specific least-work through-going fault path, the superposition of faults from a short series of time steps gives a better idea of the range of active faults during any period.

Topographic increments (Δh) above ramps in the path at each step are given by the expression $\Delta h = \Delta x \sin\theta / |\cos\theta|$, where the $|\cos\theta|$ is an area-preserving correction term accounting for kink geometries (Masek and Duncan, 1998). Since the new topography changes both the gravitational and frictional work configuration of the next time step, the minimum-work path may change, resulting in a dynamic model in which the topographic evolution is tightly

coupled to the evolution of fault paths. For simplicity, we do not deform or translate the grid (or any prior fault paths) during the "deformation".

To simulate rheological changes along the modeled profile (e.g., décollement levels), user-defined areas with different coefficients of friction can be established inside the grid. We included a strain weakening term (sw) reproducing the progressive weakening that real faults suffer during slip, such that the effective friction coefficient of a segment that has previously slipped (μ') is inversely proportional to the number of times that segment has slipped (N):

$$\mu' = \mu \left[sw + \frac{(1 - sw)}{(1 + N)} \right] \tag{2}$$

Finally, a general orogen-scale erosion is implemented, following the approach outlined by Whipple and Meade (2004, 2006). At each step, the width and slope of the model wedge is measured. Specifying a, b, and C parameters, we compute mean erosion according to

$$\overline{E} = C(\tan \alpha)^b W^a \tag{3}$$

where C is the erosion rate constant (m^{1-a}/yr; set by climate, rock properties, and channel characteristics), α denotes the taper angle of the mean topography of the wedge, W is wedge width, and a and b are positive constants set primarily by the physics of river incision (how non-linear, threshold effects, etc) and network geometry (Hack's law) (Whipple and Meade, 2004). Eq. (3) gives the average erosion rate. We allow erosion rate to vary with position according to a power–law relation following Whipple and Meade (2004):

$$E(x) = \gamma(W - x)^c \tag{4}$$

with the constraint that the erosion intensity (γ) parameter must be set to yield the same mean value ($\overline{E}$) calculated with Eq. (3). The coefficient C in Eq. (3) and the exponent (c) in Eq. (4) are settable model parameters. Climate (and rock type) are only expected to influence C - the erosion rate constant - not the values of the exponents in Eq. (3) (a, b) (Whipple and Meade, 2004). We follow Dahlen and Barr (1989) and Dahlen and Suppe (1988) in using $a = b = 1$ in all cases. We choose $a = b = 1$ as this represents the well-known linear unit stream power river incision model and typical drainage basin shapes (Whipple and Meade, 2004). We also note that with $a = b = 1$, Eq. (3) simplifies to $E \sim$ Relief, a relation for which there is much empirical support (e.g., Ahnert, 1970; Pazzaglia et al., 1998; Whipple and Meade, 2004). Following Whipple and Meade (2006) we further assume that Eq. (3) applies during the transient adjustment of orogen size, consistent with self-similar wedge growth and decay.

3. Model scenarios

In all models presented here we vary the erosional efficiency (C in Eq. (3)), while all other geometric constraints and boundary conditions are held constant (Table 1 and Fig. 2). This strategy permits isolating the effects of the erosional efficiency (i.e., climate

Table 1
Model parameters: *d.l.*, décollement level; *Sh.*, shortening applied; *μ*, friction coefficient; *S.w.*, strain weakening; *C*, coefficient of erosional efficiency (Eq. (3)). 6000 steps have been run.

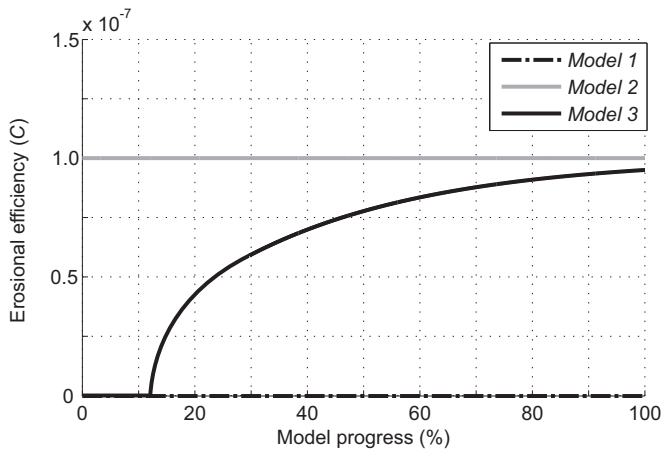|	Start node	d.l. (km)	Sh. (km)	Sh./step (m)	μ_{grid}	$\mu_{d.l.}$	S.w.	C vs. time
1	LL corner (−25 km)	−10	60	10	0.2	μ/4	0.9	0 (No erosion)
2	LL corner (−25 km)	−10	60	10	0.2	μ/4	0.9	1×10^{-7}
3	LL corner (−25 km)	−10	60	10	0.2	μ/4	0.9	Exponential recovery asymptotic to 1×10^{-7}

Fig. 2. Erosional efficiency (C in Eq. (3)) as a function of model progress for each modeled climatic setting.

and rock type) from other inputs. For those models with erosion (models 2 and 3), we set erosion rate to increase linearly toward the wedge toe ($c = 1$ in Eq. (4)). For Model 3, a temporal increase of erosional efficiency has been included, as shown in Fig. 2. Although sedimentation may both inhibit internal deformation, and promote frontal accretion when material does not leave the system (e.g., Stockmal et al., 2007), for simplicity, we assume that all eroded material leaves the synthetic profile. This is in fact a good first-order approximation for the natural example considered here, the SSA, which has seen an increase in bypassing sediments to the foreland Chaco basin since Miocene times (Uba et al., 2005).

The first model of thrust belt growth (Model 1) was run without incorporating erosion, and is used as a reference to compare with other simulations including erosion. Model 2 was run under fixed erosive conditions (erosional efficiency remaining steady with time according to Eq. (4)), simulating a steady climate scenario. Model 3, in turn, explores belt growth developed when erosivity is steadily increasing (Fig. 2), due, e.g., to increasing precipitation or discharge variability, as may have been the case along the Subandean ranges since late Miocene (Uba et al., 2005, 2006; Ege, 2004; Barnes et al., 2006; Mulch et al., 2010). The timing of when C starts to increase makes little difference to the overall response.

Our models are best described defining two fundamental metrics associated with an active orogenic wedge (Fig. 3), namely: W_a (the 'active width', defined as the zone of potential fault activity at any given instant in time during the wedge's evolution) and W_t (the 'total' width, defined as the distance from the wedge's deformation front to its to back stop). Using these parameters, simultaneous motions on a series of thrusts may be described and analyzed, in place of the in- and out-of-sequence faulting concept.

Although considerable natural variations exist among fold-and-thrust belts and accretionary wedges, several common structural
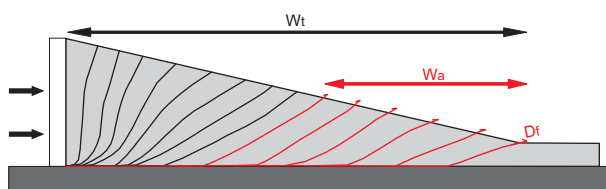

Fig. 3. Schematic diagram illustrating the parameters discussed in the text: W_a (active width, defined as the zone of potential fault activity at any given instant in time during the wedge's evolution); W_t (total width, defined as the distance from the wedge's deformation front and its back); and Df (Deformation front).

properties occur in cross section: a few large fault zones root into the hinterland basement, while a greater number splay toward the surface in an imbricate fan structure, commonly rooted in a shallow décollement (e.g., Cook and Varsek, 1994). In order to establish this standard tectonic configuration, we opted for a uniform crustal friction ($\mu = 0.2$) for most of the pre-deformation modeling grid. This value is lower than Byerlee's universal value of 0.85 for most rocks, although it is in good agreement with experimental results (Logan and Rauenzahn, 1987; Collettini et al., 2009), and with published values for the San Andreas system (Mount and Suppe, 1987; Bird and Kong, 1994). Masek and Duncan (1998) found that only with such low values for the friction coefficient can this class of model generate reasonable values for wedge slopes (i.e. $< 15°$). They are, though, in the same order of magnitude and therefore are suitable for our main interest of understanding relationships, trends and magnitudes of structural responses and to investigate the physical controls on fault activity in the wedge.

We located the start node for the fault trajectories in the lower left corner of the profile, at 25 km depth. Towards the 'foreland' a horizontal trajectory 10 km below the surface of the grid defines a weak décollement level, bearing a friction coefficient $\mu_{d.l.} = \mu/4$ (Fig. 4 and Table 1). The typically gentle hinterlandward dip of this level (only $2-3°$ W for the SSA, e.g., Echavarria et al., 2003) can be neglected. We apply small incremental shortenings ($\Delta x = 10$ m per time step); this is realistic for the purpose of our models, given that we intend that the superposition of faults from a short series of time steps renders a good idea of the complete range of active faults during a given period. We applied a total of 6000 increments (60 km of total shortening), assuming therefore a nominal shortening rate of 0.5 cm/yr, where each time step represents ~2000 years. In all cases, the initial crustal section was 25 km × 220 km, with a vertical node spacing of 2 km, a horizontal node spacing of 4 km, initially flat topography, and ten possible exit directions (5 to the left and 5 to the right, including the horizontal links).

Each climate scenario was associated with a different erosional efficiency, which may vary within at least three orders of magnitude (Stock and Montgomery, 1999). Whipple (2004) has recently reviewed the current understanding of the several controls on erosional efficiency, pointing out the difficulty of quantitatively relating this parameter to measurable climatic and lithologic properties. Aware of this, we assumed a range of values (Table 1) leading to steady-state scenarios, and permitting us to examine the temporal evolution of the models. The applied values are within the range found by Stock and Montgomery (1999), and are consistent with typical stream power river incision model parameters (Whipple and Meade, 2004).

4. Results

4.1. No erosion (Model 1)

As mentioned in Section 3, this simulation serves as a base reference, serving to reveal the role of erosion patterns applied in the other models. During the initial deep rooted (thick-skinned) deformation stage (Fig. 4a), the surface rupture (i.e. the point where the fault path exits the top of the grid) migrates consistently toward the foreland. As topographic uplift proceeds, the faults prefer longer paths which avoid uplifting existing topography, thus reducing gravitational work, although paying a cost in terms of frictional work. As the fault trajectories reach the décollement, they experience a lower average friction and the belt evolves by thin-skinned deformation. The transition between the two structural styles is reflected by a pronounced break in topographic slope, as expected from critical taper theory (Dahlen, 1990) (Fig. 4b). As thin-skinned thrusting evolves, the surface rupture
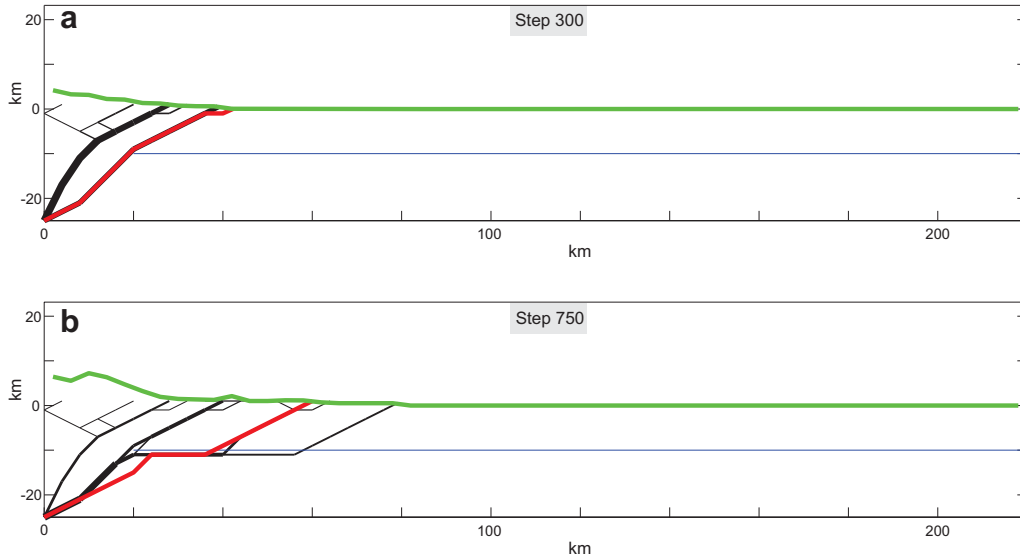
Fig. 4. Model 1 results. Blue line: low friction (25% of rest of the grid) décollement level. Fault paths are shown with line thickness scaled in proportion to the number times of activation on that segment. Active structure for each step is shown in red. (a) episode of the inner thick-skinned deformation stage, with a progressive advance of the deformation front; (b) episode of the succeeding thin-skinned deformation stage, showing a characteristic backward jump of the active fault path. (For interpretation of the references to colour in this caption, the reader is referred to the web version of this article.)

begins occasionally to jump backward (Fig. 4b). Strain weakening (Table 1) induces faults to choose the same path repeatedly, building a rough topography with local depressions. This in turn generates jumps in fault-path surface rupture locations along the profile, in response to the variable loading condition. Although a general forward accretion sequence prevails, a significant amount of internal deformation exists at any given time during the evolution of the wedge. The resulting fault pattern is a rather uniform spread along the profile (Fig. 5a_1 and a_2), reflected by a W_a ranging between 70 and 80% of the W_t at the end of the run. Similar behavior has been observed in more complex finite element models (Stockmal et al., 2007), where local structurally induced deviations from the taper critical angle promotes wedge internal

deformation, and is required in order for wedges to grow in a self-similar pattern, maintaining critical taper.

4.2. Steady erosional efficiency (Model 2)

Fig. 5b_1 shows that under fixed erosional efficiency, the frontal advance of the wedge-front is inhibited, reaching a steady state after a given amount of forward propagation. From almost the mid-point of the model evolution, all the applied shortening is consumed by surface ruptures over a narrow frontal zone comprising ~20% of the W_t. The resulting focused active deformation width (W_a) contrasts with the widely distributed one obtained without erosion (Model 1; compare Fig. 5a_1 and b_1). In Model 2 the
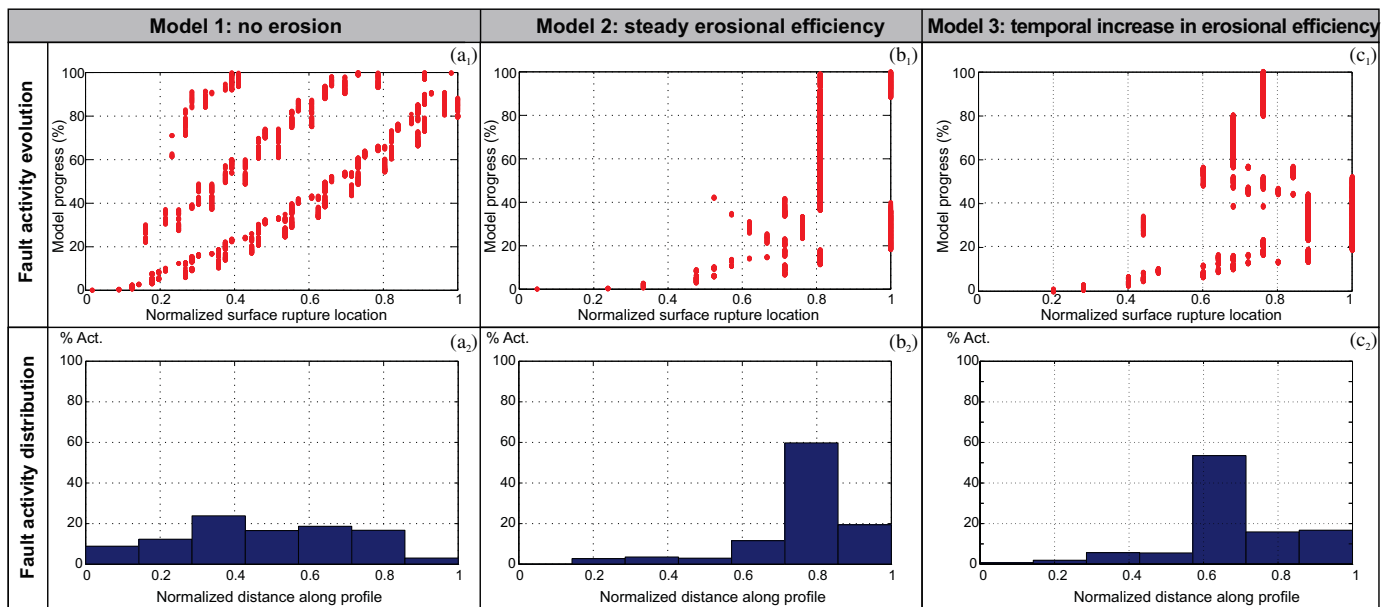

Fig. 5. Comparative evolution plots for models 1, 2 and 3 (first, second and third column respectively). (a_1), (b_1) & (c_1) Model progress vs. location of surface thrust ruptures, normalized to the farthest position reached by the deformation front; (a_2), (b_2) & (c_2) normalized fault rupture density along the profile for whole model evolution.
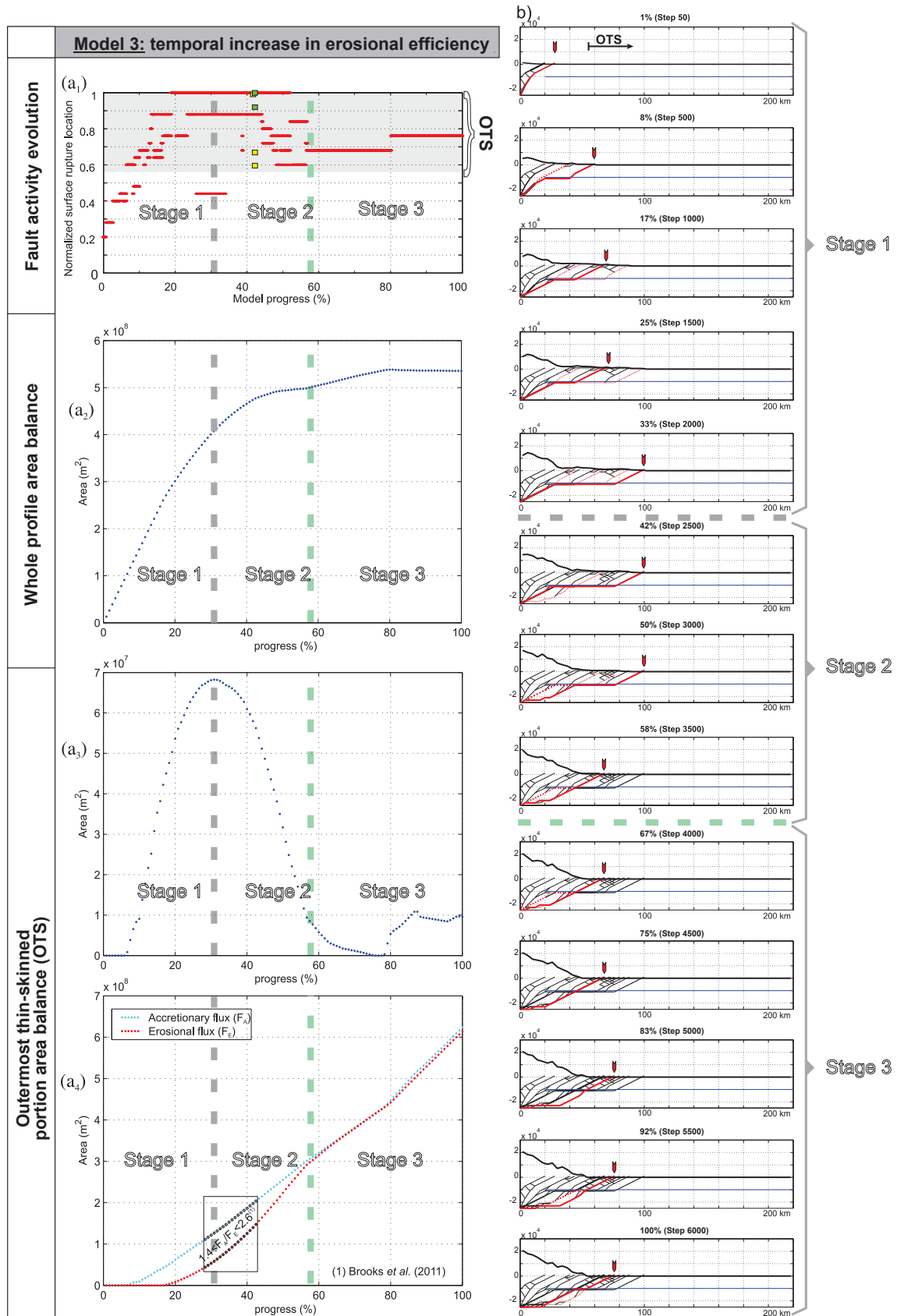
Fig. 6. a) Model 3 (temporal increase in erosional efficiency) plots; gray and green dashed lines delimitate stages 1, 2 and 3, discussed in the text; (a₁) Model progress vs. normalized location of surface thrust ruptures, overlaid with the location of active structures along the SSA profile (normalized to the farthest position reached by the deformation front). Green squares: active thrusts since Uba et al. (2009); yellow squares: active thrusts since Mugnier et al. (2006). Gray shadow highlights the referred 'outermost thin-skinned' (OTS) portion of the profile shown in Fig. 6b; (a₂) Model progress vs. Whole profile area plot (equivalent to mass flux in 3D); (a₃) Model progress vs. OTS profile area plot; (a₄) Model progress vs.

balance reached between tectonic mass influx and erosive mass efflux limits the outward growth of the wedge and generates a regular topographic profile, in agreement with analytical solutions (Whipple and Meade, 2004; Roe et al., 2006). Furthermore, the internal wedge deformation is inhibited, and thrust activity remains stationary at the wedge front, owing to the increase in erosion rate established toward the wedge toe ($c = 1$ in Eq. (4)). The resulting distribution of fault activity is shown in Fig. 5b$_2$.

4.3. Temporal increase in erosional efficiency (Model 3)

This model (Table 1) was performed in order to simulate orogenic wedge construction under increasing erosional efficiency (presumably a consequence of growing orographically-enhanced precipitation rates), as has been associated with the Subandean ranges since late Miocene (Uba et al., 2005, 2006; Ege, 2004; Barnes et al., 2006; Mulch et al., 2010). We concentrate on the effects of erosional efficiency changes, without introducing any other variation to the system (e.g. shortening). The results show interrelations between thrust front evolution, profile area balance, and active fault distribution, as follows.

4.3.1. Thrust front evolution

During the initial ~30% of the run, the active thrust front of the wedge propagates forward until it reaches its farthest position (Fig. 5c$_1$). From the ~30%−~60% points in elapsed run-time, deformation is absorbed by coeval activity along the previously developed, long-lasting thrust front, and along internal short-lived structures. This latter fault family displays a general backward surface rupture migration sequence, accompanying the increase in erosional efficiency. This observation is in good agreement with sandbox simulations (Hoth et al., 2006), which show considerable out-of-sequence deformation amplified by erosion during a general forward-breaking thrust sequence. Finally (~60% to the end of the run) all the activity is consumed along a steady and narrow section of the wedge located at about 75% of its total length (Fig. 5c$_1$). The resulting whole-run fault rupture distribution pattern shows a maximum concentration along the mentioned section, whereas a complementary sparse activity occupies the frontal segment of the system (Fig. 5c$_2$).

4.3.2. Profile area balance and distribution of fault activity

The three above-mentioned stages of evolution for Model 3 can be best delimited and understood by correlating each with its corresponding profile area balance (equivalent to mass balance in 3D). Since we aim to compare our findings with the SSA, for which we have mass balance estimates (Brooks et al., 2011), it is appropriate to calculate the area balance for the outermost thin-skinned (OTS) segment of the model, separately from the whole profile (WP) (Fig. 6).

Stage 1, in both WP and OTS, is marked by an area increase, which likely results from the progressive outward migration of the thrust front, and the concurrent incorporation of material via frontal accretion at the toe of the growing wedge (Fig. 6a$_1$). The maximum OTS area corresponds to the maximum advance of the wedge's deformation front (maximum W_t; see Fig. 6b). The progressive forward migration of the thrust activity during this stage gives rise to a rather uniform fault rupture density along the profile (Fig. 7a).

After reaching this maximum, the rising erosional efficiency induces the wedge to shrink by decreasing the area of the OTS, and generates a pronounced slowdown in the rate of WP area growth (Stage 2; Fig. 6a$_2$ and a$_3$). This flux balance occurs concomitantly with hinterlandward thrust rupture migration, restricted to the OTS section of the profile (Fig. 6a$_1$ and a$_3$). It is noteworthy that the activity at the deformation front does not terminate during the initial part of this retreat, and therefore a W_a consisting of multiple active thrusts is established. W_a comprises ~40−50% of the total profile width (Fig. 7b), but more than the 75% of the fault ruptures concentrate on the frontal ~30% section. This re-configuration pattern of active structures responds to the OTS area decrease characterizing Stage 2, at which transient non-steady mass balance conditions still favors accretionary flux (Fig. 6a$_3$ and a$_4$).

During the final stage of the model (Stage 3), an almost neutral area balance for both WP and OTS is reached (Fig. 6a$_2$−a$_4$), dictating a steady state (erosional efflux equal to accretionary influx, Willett and Brandon, 2002). An area increase is registered, though, at ~80% of model evolution, responding to the frontal propagation of the deeper segment of the fault-path (basal accretion; Fig. 6a$_3$ and b). The fault rupture distribution is also stationary, covering a narrow W_a behind the previously reached thrust front maximum (Fig. 6a$_1$, b). Fig. 7c highlights this sharp localization, where ~10% of the W_t accounts for all the shortening applied during this stage.

The described retreat of the active deformation front, and the following strain concentration within the wedge interior, confirm the expected narrowing of an orogenic wedge after an erosional efficiency increase, predicted both by analytical and numerical approaches (Whipple and Meade, 2004, 2006; Stolar et al., 2006; Simpson, 2006; Whipple, 2009). The final steady mass flux conditions reached (Stage 3) favor the localized deformation attained, given the spatial increase in erosion rate toward the toe of the wedge. The previous deformation front retreat process is associated with a more diffuse fault activity distribution, responding to the transient non-steady mass balance (Stage 2). Even so, this re-configuration pattern still involves a higher active faulting concentration on the frontal section of the wedge (Fig. 7b).

5. Discussion and application to the Southern Bolivian Subandes

The natural prototype considered for the application of the models is the SSA, an orogenic segment characterized by thin-skinned thrusting, where erosion appears to have modulated its tectonic evolution (e.g., Leturmy et al., 2000; Barnes et al., 2006; Uba et al., 2009). We believe that our numerical simulations provide valuable elements for more complete understanding of the effects of variable erosional settings on long-term, whole-wedge deformation patterns. A better understanding of the factors controlling the respective contribution of accumulated slip propagating to the thrust front, versus activation of any other structure in the locked zone, is key for interpreting the seismotectonic behavior of the SSA.

5.1. The Southern Bolivian Subandes

The Subandean fold and thrust belt of the Central Andes (Fig. 8) is a classical example of active thin-skinned deformation (Dunn et al., 1995; Moretti et al., 1996; Baby et al., 1997; Echavarria

OTS accretionary (blue) and erosional (red) flux; note their overlap during Stage 3. Boxed area shows the same range of area flux ratios (*FA/FE*) estimated for the SSA (Brooks et al., 2011a) in our modeled flux ratios; *FA* (Accretionary flux); *FE* (Erosional flux). b) Model evolution, separated in the three defined stages. Red solid lines, active fault-paths. Red dotted lines, fault-paths active during five steps previous to the one shown. (For interpretation of the references to colour in this figure legend, the reader is referred to the web version of this article.)
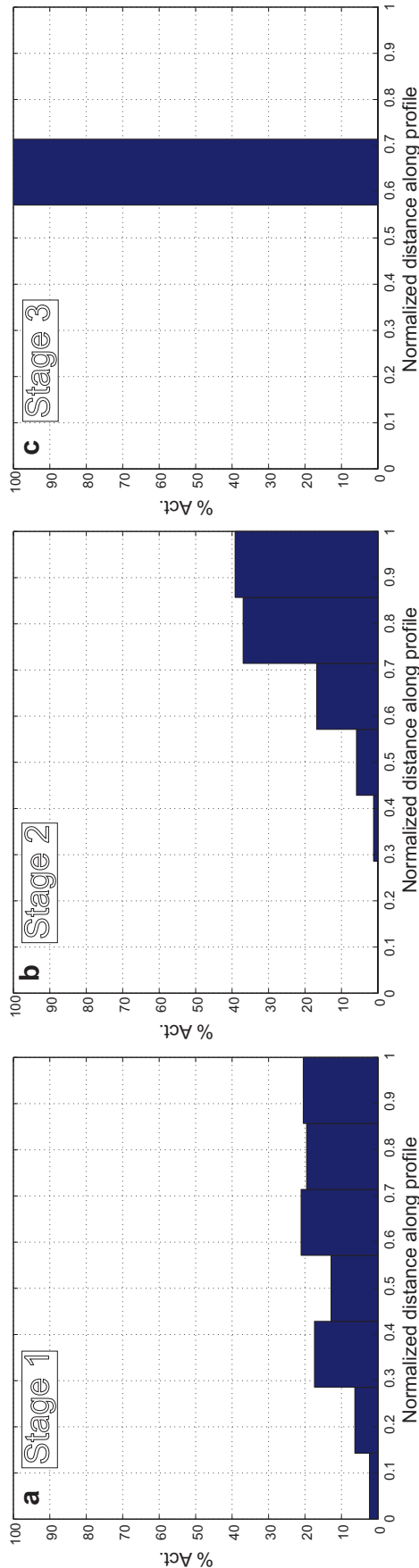
Fig. 7. Fault ruptures density plots for (a) stage 1, (b) stage 2 and (c) stage 3 of Model 3.

et al., 2003), forming the external border of the Andean chain. It extends for about 600 km from the Bolivian orocline's "elbow" at Santa Cruz de la Sierra to northwestern Argentina. In a general way, all the major thrust faults are E-vergent and root in a regional basal décollement primarily in Silurian strata, deforming a 6−12 km thick pile of Paleozoic marine sediments to Tertiary strata (Dunn et al., 1995; Baby et al., 1992; Belotti et al., 1995; Leturmy et al., 2000; Echavarria et al., 2003). This décollement projects beneath the hinterlandward high topography of the Andean/sub-Andean boundary (Inter-Andean zone in Fig. 8; Allmendinger and Zapata, 2000), forming duplexes of Precambrian units at mid-crustal depths with roof décollements in the Silurian horizon (Dunn et al., 1995; Allmendinger and Zapata, 1996; Baby et al., 1997; McQuarrie and DeCelles, 2001).

The SSA has expanded in width during the last ~12 My by means of cratonward propagation of the wedge tip (Uba et al., 2009). Balanced cross sections indicate total shortening of ~60 km (Dunn et al., 1995; Echavarria et al., 2003; Uba et al., 2009). Most of the deformation suffered a westward retreat from late Miocene to present (Echavarria et al., 2003; Uba et al., 2009; Mugnier et al., 2006), whose causes are still under debate (Echavarria et al., 2003; Uba et al., 2009). During this pulse (beginning at ~4.5 Ma) all of the thrust sheets across an ~100 km-wide-zone were simultaneously active (Echavarria et al., 2003; Ramos et al., 2004). Mosquera (1999) has identified at least two syngrowth sequences associated with pulses of out-of-sequence thrusting dated at 2−1.5 Ma and 1.5−0.25 in the southern continuation of Suaruro thrust (Fig. 8). Correlative syngrowth sequences were recognized on both limbs of Sierra de Aguaragüe (Mosquera, 1999). Even farther east, the Mandeyapecua thrust, a new active structure, was developing within this time interval (Uba et al., 2009).

Although the early GPS measurements in the backarc suggested that the SSA is not undergoing internal shortening (Bevis et al., 2001) data were spatially sparse, and the interpretation regarding wedge-specific processes is therefore limited. New data demonstrate a sharp backarc velocity gradient from ~10 to ~2 mm/yr over the outermost ~25−100 km (Fig. 8; Brooks et al., 2011). This velocity gradient has been modeled by Brooks et al. (2011) as a single subhorizontal dislocation in an elastic half-space slipping freely in the west, but locked for up to ~100 km in shallower sections further east. Two key unanswered questions are addressed in this paper through analogies with the described minimum-work models, namely: (1) where along the wedge is this shortening most probably accommodated over both geologic and neotectonic timescales, and (2) what are the physical factors governing this location.

All different approaches to the problem of Subandean deformation propose that structures other than those at the wedge front are currently active (Echavarria et al., 2003; Lamb, 2000; Mugnier et al., 2006; Uba et al., 2009). Drainage patterns evidencing rapid dissection on the hanging walls of the Aguaragüe and the ~500 km long Mandeyapecua thrusts (Fig. 8) have been described by Lamb (2000). Likewise, evidence of active faulting was found along the Río Pilcomayo (the main river that crosses the Subandean thrust belt at ~21° SL) associated to the Aguaragüe and the Suaruro internal SSA thrusts (Mugnier et al., 2006). Based on morphological indicators, these authors estimated that more than half of the 10 ± 3 mm/yr of total long-term shortening rate is being taken up through the internal Aguarague structure, located ~50 km to the west of the emerging front of the system (Mandeyapecua thrust). According to their calculations, the latter structure would be only weakly active (Fig. 8). The resulting W_a of this section of the SSA would thus be between ~100 km (considering that the Suaruro thrust is active) and ~50 km (taking the Aguaragüe thrust as the only internal active structure). We consider this last option as the most reliable, given that the activity along the Aguarague structure
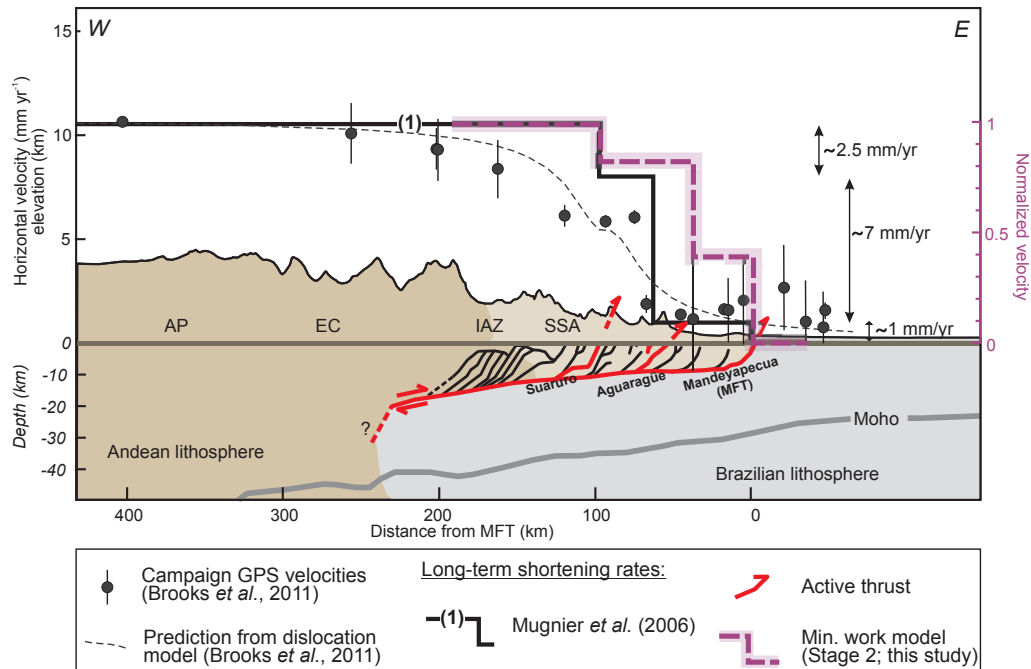
Fig. 8. Structural cross-section across the Bolivian Central Andes at 20° S (Dunn et al., 1995), showing the major structures; *MFT* (Mandeyapecua Frontal Thrust). Several geographical domains are distinguished; *AP*, Andean Plateau; *EC*, Eastern Cordillera; *IAZ*, Inter-Andean zone; *SSA*, southern Subandes. Geodetic velocities (black dots), dislocation model velocity curve (gray dashed line) (Brooks et al., 2011) and estimated long-term velocities across SSA (Mugnier et al., 2006). Normalized velocity curve for Stage2 of Model 3 (purple dashed line), developed under transient unbalanced area flux conditions. (For interpretation of the references to colour in this figure legend, the reader is referred to the web version of this article.)

is further supported by the presence of associated eroded hanging wall terraces in Bolivia (Lamb, 2000) and growth strata patterns on its backlimb in northern Argentina (Echavarria et al., 2003).

The climate of the Subandean ranges appears to have shifted towards more humid conditions since the late Miocene (Uba et al., 2005, 2006; Mulch et al., 2010), resulting in a high sediment accumulation that rapidly filled the accommodation space, and may have promoted an increased bypassing of sediment (Uba et al., 2005, 2009). This climate-driven increase in erosive processes is in line with thermochronologic studies (e.g., Ege, 2004; Barnes et al., 2006). However, mass balance analyses suggest that accretionary flux (F_A) is larger than erosional flux (F_E) from SSA-wide denudation rates (Insel et al., 2010), indicating a transient unbalanced condition (non-steady state) over time periods of $10^2 - 10^6$ yr (Fig. 6a$_4$; Brooks et al., 2011).

5.2. Comparison of models and the Southern Bolivian Subandes

Our Model 3 simulation settings were established in order to explore the effects of increasing erosional efficiency conditions on the distribution of fault activity along an active thin-skinned fold and thrust belt; therefore, it constitutes a suitable analogue to the SSA growth. The general backward surface rupture migration sequence developed during this stage (Fig. 6a$_1$) compares well with the westward fault activity retreat identified in the SSA from late Miocene to present (Echavarria et al., 2003; Ramos et al., 2004; Uba et al., 2009; Mugnier et al., 2006).

Highlighting the range of area flux ratios (FA/FE) estimated by Brooks et al. (2011) for the SSA in our model's OTS area balance plot, we find that it falls within Stage 2 values (Fig. 6a$_4$). A good agreement is further obtained if we compare the normalized location of active structures along the SSA profile (Fig. 6a$_1$; green squares since Uba et al., 2009; yellow squares since Mugnier et al., 2006), with the modeled surface ruptures distribution developed during the

time span of interest ($1.4 < FA/FE < 2.6$; Brooks et al., 2011). Such correspondence points out that the currently unbalanced mass flux conditions may be promoting the observed active structural setting. This pattern is, in turn, markedly different from that of Stage 3 (compare Fig. 7b and c), characterized by a sharply localized W_a, dictated by a steady balanced mass flux. Therefore, our analysis supports the notion that the SSA is not in steady state, but it is rather responding to an erosional efficiency increase since late Miocene by means of active thrusting on the frontal section of the wedge, coeval with internal short-lived structures.

A synthetic velocity plot for Stage 2 of Model 3 has been constructed (Fig. 8): we first discretized the profile assuming three active discontinuities, as proposed by Mugnier et al. (2006) for the SSA. Then we computed the normalized velocity for each defined block according to the fault rupture distribution relative to established block limits. The distinctive stair-stepped geometry obtained, associated with internal deformation occurring along the growing wedge, replicates the natural long-term shortening curve. However, the predicted velocity on the front of the synthetic wedge is significantly higher than the one estimated on the Mandeyapecua frontal thrust by Mugnier et al. (2006).

6. Conclusions

Minimum-work wedge simulations presented in this study lead to a number of interesting predictions that could be tested observationally, highlighting unresolved aspects of the roles of erosion and its temporal variability in modulating the location and evolution of thrusting. This approach augments traditional critical wedge theory by allowing us to evaluate the fault distribution pattern through time.

All three model scenarios exhibit contrasting fault activity distributions (Fig. 5), depending on the applied erosional settings, as summarized:

a) Under hyper-arid conditions (no erosion, Model 1) a continuous forward thrust front migration is obtained; yet the rough topographic profile built induces systematic backward jumps of the surface ruptures. This gives rise in turn to a wide distribution of thrust activity, reflected by a W_a ranging between 70 and 80% of W_t by the end of the run.

b) Under a fixed erosional efficiency (Model 2) a steady state is reached: the fault-path surface ruptures migrate towards the foreland, remaining localized at the wedge tip. A narrow long-lived active frontal zone comprising the outermost ~20% of the W_t is established.

c) Under a temporal increase in erosional efficiency (Model 3) three stages with distinct profile-area flux balance conditions are recognized, and can be correlated with a given structural response (Fig. 6):

- Stage 1 is marked by an area increase along both the whole profile (WP) and the outermost thin-skinned (OTS) segment of the model, which likely results from the progressive outward migration of the thrust front.

- Stage 2 is characterized by a transient OTS area decrease, accompanied by coeval thrust activity at the front and at internal fringes of the profile (Fig. 6a$_1$, a$_3$ and b). The W_a comprises ~40–50% of the total profile width (Fig. 7b), but more than the 75% of the fault ruptures concentrates on the frontal ~30% section. This structural pattern responds to the OTS area decrease.

- Stage 3 is marked by the achievement of steady-state area flux conditions, promoting the development of a single long-lived deformation front, while duplexing by basal accretion occurs at deep structural levels (Fig. 6b). Only ~10% of the W_t accounts for all the shortening applied during this stage.

The results of Model 3 confirm the expected narrowing of an orogenic wedge after an increase of erosional efficiency. A remarkable result of this simulation is the rather diffuse distribution of fault activity observed during the retreat of the deformation front, differing from the steady and sharply localized one of the final stage.

The analogy drawn with the SSA ranges permits us to speculate that a transient non-steady state (FA > FE) drives the system towards synchronous activity at the thrust front, and at internal thrusts splaying from the décollement. Such interpretation, based on model predictions, supports indirect evidences of active deformation associated with internal SSA structures (Suaruro and Aguaragüe thrusts). More information on the long-term slip rates across both the frontal and inner active thrusts of the SSA is still needed in order to estimate their respective contribution to whole-wedge deformation.

The reported results shed light on the impact of different mass balance conditions on the vastly different kinematics found in mountain ranges, suggesting that those affected by growing erosion under a transient unbalanced mass flux condition (FA > FE) tend to distribute deformation along both frontal and internal faults, while others, under balanced conditions, would focus deformation on a limited number of persistent structures.

Acknowledgments

References

Adam, J.J.L., Urai, B., Wieneke, O., Oncken, K., Pfeiffer, N., Kukowski, J., Lohrmann, S., Hoth, W., van der Zee, J., Schmatz, J., 2005. Shear localization and strain distribution during tectonic faulting-new insights from granular-flow experiments and high resolution optical image correlation techniques. J. Struct. Geol. 27, 283–301.

Ahnert, F., 1970. Functional relationships between denudation, relief, and uplift in large mid-latitude drainage basins. Am. J. Sci. 268, 243–263.

Allmendinger, R.W., Zapata, T.R., 1996. Imaging the Andean structure of the Eastern Cordillera on reprocessed YPF seismic reflection data. Congr. Geol. Argent. 8 (2), 125–134.

Allmendinger, R.W., Zapata, T.R., 2000. The footwall ramp of the Subandean décollement, northernmost Argentina, from extended correlation of seismic reflection data. Tectonophysics 321, 37–55.

Baby, P., Herail, G., Salinas, R., Sempere, T., 1992. Geometry and kinematic evolution of passive roof duplexes deduced from section balancing: example from de foreland thrust system of the southern Bolivia Subandean Zone. Tectonics 11, 523–536.

Baby, P., Rochat, P., Mascle, G., Hérail, G., 1997. Neogene shortening contribution to crustal thickening in the back arc of the Central Andes. Geology 25, 883–886.

Barnes, J.B., Ehlers, T.A., McQuarrie, N., O'Sullivan, P.B., Pelletier, J.D., 2006. Eocene to recent variations in erosion across the central Andean fold-thrust belt, northern Bolivia: implications for plateau evolution. Earth Planet. Sci. Lett. 248, 118–133.

Barr, T.D., Dahlen, F.A., McPhail, D.C., 1991. Brittle frictional mountain building: 3. Low-grade metamorphism. J. Geophys. Res. 96, 10,319–10,338.

Beaumont, C., Jamieson, R.A., Nguyen, M.H., Lee, B., 2001. Himalayan tectonics explained by extrusion of a low-viscosity channel coupled to focused surface denudation. Nature 414, 738–742.

Belotti, H., Saccavino, L., Schachner, G., 1995. Structural styles and petroleum occurrence of the Sub-Andean thrust belt. of northern Argentina. In: Tankard, A.J., et al. (Eds.), Petroleum Basins of South America: American Association of Petroleum Geologists Memoir 62, pp. 545–555.

Bevis, M., Kendrick, E., Smalley Jr., R., Brooks, B.A., Allmendinger, R.W., Isacks, B.L., 2001. On the strength of interplate coupling and the rate of back arc convergence in the central Andes; an analysis of the interseismic velocity field. Geochem. Geophys. Geosyst. 2 http://dx.doi.org/10.129/2001GC000198.

Bird, P., Kong, X., 1994. Computer simulations of California tectonics confirm very low strengths of major faults. Geol. Soc. Am. Bull. 106, 159–174.

Brooks, B.A., Bevis, M., Whipple, K., Arrowsmith, J.R., Foster, J., Zapata, T., Kendrick, E., Minaya, E., Echalar, A., Blanco, M., Euillades, P., Sandoval, M., Smalley Jr., R., 2011. Orogenic wedge deformation and potential for great earthquakes in the central Andean backarc. Nat. Geosci. 4 (6), 380–383.

Collettini, C., Niemeijer, A., Viti, C., Marone, C., 2009. Fault zone fabric and fault weakness. Nature 462, 907–910. http://dx.doi.org/10.1038/nature08585.

Cook, F.A., Varsek, J.L., 1994. Orogen-scale decollements. Rev. Geophys. 32, 37–60. http://dx.doi.org/10.1029/93RG02515.

Cooke, M.L., Murphy, S., 2004. Assessing the work budget and efficiency of fault systems using mechanical models. J. Geophys. Res. 109, B10408. http://dx.doi.org/10.1029/2004JB002968.

Cubas, N., Leroy, Y.M., Maillot, B., 2008. Prediction of thrusting sequences in accretionary wedges. J. Geophys. Res., B12412. http://dx.doi.org/10.1029/2008JB005717.

Dahlen, F.A., 1990. Critical taper model of fold-and-thrust belts and accretionary wedges. Annu. Rev. Earth Planet. Sci. 18, 55–99.

Dahlen, F.A., Barr Jr., T.D., 1989. Brittle frictional mountain building: 1. Deformation and mechanical energy balance. J. Geophys. Res. 94, 3906–3922.

Dahlen, F.A., Suppe, J., 1988. Mechanics, growth, and erosion of mountain belts. In: Clark, S.P.J., Burchfiel, B.C., Suppe, J. (Eds.), Processes in Continental Lithospheric Deformation. Geol. Soc. of Am., Denver, Colo, pp. 161–178.

Del Castello, M., Cooke, M.L., 2007. Underthrusting-accretion cycle: work budget as revealed by the boundary element method. J. Geophys. Res. (Solid Earth). http://dx.doi.org/10.1029/2007JB004997.

Dunn, J.F., Hartshorn, K.G., Hartshorn, P.W., 1995. Structural styles and hydrocarbon potential of the Subandean thrust belt of southern Bolivia. In: Tankard, A.J., et al. (Eds.), Petroleum Basins of South America: American Association of Petroleum Geologists Memoir 62, pp. 523–543.

Echavarria, L., Hernandez, R., Allmendinger, R., Reynolds, J., 2003. Subandean thrust and fold belt of northwestern Argentina; geometry and timing of the Andean evolution. AAPG Bull. 87 (6), 965–985.

Ege, H., 2004. Exhumations- und Hebungsgeschichte der zentralen Anden in Südbolivien (21°S) durch Spaltspur-Thermochronologie an Apatit. Ph.D. Thesis. Freie Universität Berlin, Berlin.

Finlayson, B.A., Scriven, L.E., 1967. On the search for variational principles. Lnt. J. Heat Mass Transf. 10, 799–822.

Gutscher, M.A., Kukowski, N., Malavieille, J., Lallemand, S., 1996. Cyclical behavior of thrust wedges: insight from high basal friction sandbox experiments. Geology 24, 135–138.

Hardy, S., Duncan, C., Masek, J., Brown, D., 1998. Minimum work, fault activity and the growth of critical wedges in fold and thrust belts. Basin Res. 10, 365–373.

Hilley, G.E., Strecker, M.R., 2004. Steady state erosion of critical Coulomb wedges with applications to Taiwan and the Himalaya. J. Geophys. Res. 109, B01411. http://dx.doi.org/10.1029/2002JB002284.

Hilley, G.E., Strecker, M.R., Ramos, V.A., 2004. Growth and erosion of fold-and-thrust belts with an application to the Aconcagua fold-and-thrust belt, Argentina. J. Geophys. Res. 109, B01410. http://dx.doi.org/10.1029/2002JB002282.

Hoth, S., Adam, J., Kukowski, N., Oncken, O., 2006. Influence of erosion on the kinematics of bivergent orogens: results from scaled sandbox simulations. In: Willett, S.D., Hovius, N., Brandon, M.T., Fisher, D.M. (Eds.), Tectonics, Climate, and Landscape Evolution, pp. 201—225. Geol. Soc. Am. Spec. Paper, 398. Penrose Conference Series.

Insel, N., Ehlers, T.A., Schaller, M., Barnes, J.B., Tawackoli, S., Poulsen, C.J., 2010. Spatial and temporal variability in denudation across the Bolivian Andes from multiple geochronometers. Geomorphology 122, 65—77. http://dx.doi.org/10.1016/j.geomorph.2010.05.014.

Koons, P.O., 1990. Two-sided orogen; collision and erosion from the sandbox to the Southern Alps, New Zealand. Geology 18 (8), 679—682.

Lamb, S., 2000. Active deformation in the Bolivian Andes, South America. J. Geophys. Res. 105, 25,627—25,653.

Leturmy, P., Mugnier, J.L., Vinour, P., Baby, P., Colletta, B., Chabron, E., 2000. Piggyback basin development above a thin-skinned thrust belt with two detachment levels as a function of interactions between tectonic and superficial mass transfer: the case of the Subandean zone (Bolivia). Tectonophysics 320, 45—67.

Logan, J.M., Rauenzahn, K.M., 1987. Frictional dependence of gouge mixutres of quartz and montmorillonite on velocity, composition, and fabric. Tectonophysics 144, 87—108.

Mary, B., Maillot, B., Leroy, Y.M., 2013a. Deterministic chaos in frictional wedges revealed by convergence analysis. Int. J. Numer. Anal. Meth. Geomech. http://dx.doi.org/10.1002/nag.2177.

Mary, B., Maillot, B., Leroy, Y.M., 2013b. Predicting orogenic wedge styles as a function of analogue erosion law and material softening. Geochem. Geophys. Geosyst. 14 http://dx.doi.org/10.1002/ggge.20262.

Masek, J.G., Duncan, C.C., 1998. Minimum-work mountain building. J. Geophys. Res. 103 (1), 907—917.

McQuarrie, N., DeCelles, P.G., 2001. Geometry and structural evolution of the central Andean Backthrust belt, Bolivia. Tectonics 17, 203—220.

Mitra, G., Boyer, S.E., 1986. Energy balance and deformation mechanisms of duplexes. J. Struct. Geol. 8, 291—304.

Molnar, P., Lyon-Caen, H., 1988. Some simple physical aspects of the support, structure, and evolution of mountain belts. Spec. Pap. Geol. Soc. Am. 218, 179—207.

Moretti, I., Baby, P., Mendez, E., Zubieta, D., 1996. Hydrocarbon generation in relation to thrusting in the Subandean zone from 18 to 22° S, Bolivia. Petrol.Geosci. 2, 17—28.

Mosquera, A., 1999. Evolución temporal de la deformación en las Sierras Subandinas Orientales: IV° Congreso de Exploración y Desarrollo de Hidrocarburos (Mar del Plata) Actas, vol. 2, pp. 563—578.

Mount, V.S., Suppe, J., 1987. State of stress near the San Andreas fault: implications for wrench tectonics. Geology 15, 1143—1146.

Mugnier, J.L., Becel, D., and Granjeon, D., 2006. Active tectonics in the Subandean belt inferred from the morphology of the Rio Pilcomayo (Bolivia). In: Willett, S.D., Hovius, N., Brandon, M.T., and Fisher, D., eds., Tectonics, Climate, and Landscape Evolution: Geological Society of America Special Paper 398, Penrose Conference Series, pp. 353—369, doi: 10.1130/2006.2398(22).

Mulch, A., Uba, C.E., Strecker, M.R., Schoenberg, R., Page Chamberlain, C., 2010. Late Miocene climate variability and surface elevation in the central Andes. Earth Planet. Sci. Lett. 290, 173—182.

Oncken, O., Hindle, D., Kley, J., Elger, K., Victor, P., Schemmann, K., 2007. Deformation of the Central Andean upper plate system; facts, fiction, and constraints for plateau models. In: Oncken, O., et al. (Eds.), The Andes Active Subduction Orogeny. Springer, pp. 3—27.

Pazzaglia, F.J., Gardner, T.W., Merritts, D.J., 1998. Bedrock fluvial incision and longitudinal profile development over geological time scales determined by fluvial terraces. In: Tinkler, K.J., Wohl, E.E. (Eds.), Rivers Over Rocks: Fluvial Processes in Bedrock Channels, Geophys. Monogr. Ser., vol. 107. AGU, Washington, D.C, pp. 207—235.

Ramos, V.A., Zapata, T., Cristallini, E., Introcaso, A., 2004. The Andean thrust system—latitudinal variations in structural style and orogenic shortening. In: McClay, K.R. (Ed.), Thrust Tectonics and Hydrocarbon Systems: American Association of Petroleum Geologists (AAPG) Memoir 82, pp. 30—50.

Scholz, C.H., 2002. The Mechanics of Earthquakes and Faulting. Cambridge Univ. Press, New York, 472 pp.

Simpson, G.D.H., 2006. Modelling interactions between fold—thrust belt deformation, foreland flexure and surface mass transport. Basin Res. 18, 125—143.

Sleep, N.H., Stein, S., Geller, R.J., Gordon, R.G., 1979. Comment on "The use of the minimum-dissipation principle in tectonophysics" by P. Bird and D. A. Yuen. Earth Planet. Sci. Lett. 45, 218—220.

Stock, J.D., Montgomery, D.R., 1999. Geologic constraints on bedrock river incision using the stream power law. J. Geophys. Res. Solid Earth 104, 4983—4993.

Stockmal, G., Beaumont, C., Nguyen, M., Lee, B., 2007. Mechanics of thin-skinned fold-thrust belts: insights from numerical models. In: Sears, J., Harms, T., Evenchick, C. (Eds.), Whence the Mountains? Inquiries into the Evolution of Orogenic Systems: a Volume in Honor of Raymond A. Price: Geological Society of America Special Paper, vol. 433, pp. 63—98.

Stolar, D., Roe, G., Willett, S.D., 2007. Controls on the patterns of topography and erosion rate in a critical orogen. J. Geophys. Res. Earth Surf. 112, F04002.

Stolar, D.B., Willett, S.D., Roe, G.H., 2006. Climate and tectonic forcing of a critical orogen. In: Willett, S., Hovius, N., Brandon, M., Fisher, D. (Eds.), Tectonics, Climate and Landscape Evolution, GSA Special Paper 398, Penrose Conference Series, pp. 241—250.

Uba, C.E., Heubeck, C., Hulka, C., 2005. Facies analysis and basin architecture of the Neogene Subandean synorogenic wedge, southern Bolivia. Sediment. Geol. 180, 91—123.

Uba, C.E., Heubeck, C., Hulka, C., 2006. Evolution of the late Cenozoic Chaco foreland basin, Southern Bolivia. Basin Res. 18, 145—170.

Uba, C., Kley, J., Strecker, M., Schmitt, A.K., 2009. Unsteady evolution of the Bolivian Subandean thrust belt: the role of enhanced erosion and clastic wedge progradation. Earth Planet. Sci. Lett. 281, 134—146.

Vanderhaeghe, O., Medvedev, S., Fullsack, P., Beaumont, C., Jamieson, R.A., 2003. Evolution of orogenic wedges and continental plateaux: insights from crustal thermal-mechanical models overlying subducting mantle lithosphere. Int. J. Geophys. 153, 27—51.

Whipple, K., 2004. Bedrock rivers and the geomorphology of active orogens. Annu. Rev. Earth Planet. Sci. 32, 151e185.

Whipple, K., 2009. The influence of climate on the tectonic evolution of mountain belts. Nat. Geosci. 2, 97—104.

Whipple, K.X., Meade, B.J., 2004. Controls on the strength of coupling among climate, erosion, and deformation in two-sided, frictional orogenic wedges at steady state. J. Geophys. Res. 109, F01011. http://dx.doi.org/10.1029/2003JF000019.

Whipple, K.X., Meade, B.J., 2006. Orogen response to changes in climatic and tectonic forcing. Earth Planet. Sci. Lett. 243, 218—228,. http://dx.doi.org/10.1016/j.epsl.2005.12.022.

Willett, S.D., 1999. Orogeny and orography: the effects of erosion on the structure of mountain belts. J. Geophys. Res. 104 (B12), 28957—28981.

Willett, S.D., Brandon, M.T., 2002. On steady states in mountain belts. Geology 30, 175—178.

Willett, S.D., Beaumont, C., Fullsack, P., 1993. Mechanical model for the tectonics of doubly vergent compressional orogens. Geology 21, 371—374.

Williams, R.T., 1987. Energy balance for large thrust sheets and fault-bend folds. J. Struct. Geol. 9, 375—379.